IOP Publishing Journal of Optics
J. Opt. **26** (2024) 085401 (6pp) https://doi.org/10.1088/2040-8986/ad5c7d

In-plane radiation pattern generated by large particles in dielectric substrates

Juan M Merlo* and **Madeleine H Carhart**

Physics and Astronomy Department. Vassar College, 124 Raymond Ave, Poughkeepsie, NY 12604, United States of America

E-mail: jmerloramirez@vassar.edu

Received 22 April 2024, revised 31 May 2024
Accepted for publication 27 June 2024
Published 4 July 2024

Abstract

In this work we present the study of in-plane radiation patterns generated by particles with dimensions larger than the excitation wavelength. We studied the in-plane radiation of Au structures focusing on two cases: particles and triangular crystals. We found that the radiation patterns were produced by the scattering of the excitation field at the bottom edges of the studied structures. In addition, we found the in-plane radiation decay exponentially due to the refractive index contrast between the substrate and superstate. Furthermore, we proved that in-plane radiation patterns originating from different structures can interact and generate interesting geometries. Finally, in addition to our experimental studies, we show numerically calculated simulations which agreed with our experimental results and thus confirmed our findings.

Keywords: in-plane radiation, near-field microscopy, gold microparticles

1. Introduction

The study of in-plane interactions is a major research area due to its potential for on-chip manipulation of electromagnetic waves (EMWs)[1–3]. Several configurations of in-plane radiation generators have been reported to the date [4–6], with plasmonic antennas (PAs) being the protagonist of this endeavor [7–11]. In this sense, PAs have been thoroughly studied in the last two decades due to their ability to control the propagation and confinement of EMWs, with applications in sensing [7, 8], color filtering [9], and free space communication [10, 11]. It is well-accepted that a structure must have subwavelength dimensions to behave as an optical antenna [1], therefore the behavior of a subwavelength optical antenna can be explained using antenna theory with some modifications [2]. So far, studies have explored the radiation pattern generated by dipole PAs [12], horn antennas [13], Vivaldi antennas [11], and Yagi Uda antennas [14, 15], among others.

Although PAs are a good alternative for in-plane radiation control, they require precise positioning and small sizes of their components, usually of the order of tens of nanometers [15]. This results in challenging fabrication processes that do not necessarily scale up to large areas well. To date, the fabrication process of these devices is restricted to photolithography with ultraviolet wavelengths [16], and electron beam/ion beam lithography [17]. Both techniques pose important limitations for larger scale access, so new ways must be found to fabricate and control the in-plane emitters. An interesting alternative to PAs would be to use structures with dimensions larger than the excitation wavelength, which has not been reported to date. These structures can be fabricated by chemical reduction processes [18] that allow the deposition of a large number of structures, control of the size, and a large fabrication area.

This work is dedicated to studying the in-plane radiation generated by particles with dimensions larger than the wavelength of the excitation field fabricated by chemical reduction. We demonstrate that large particles with different geometries can efficiently radiate energy into their adjacent spaces. Our approach opens a new venue for potential applications in communications without the strict requirements imposed by PAs.

* Author to whom any correspondence should be addressed.

2. Experimental methods

2.1. Sample fabrication

The samples consisted of a set of crystalline Au structures (CAuS) fabricated by chemical reduction [18] and deposited by spin coating on a glass substrate. Our procedure consisted of three main steps: cleaning of the glass substrates, fabrication of a solution of CAuS in acetone, and spin coating of this solution onto the glass substrate.

The first step involved thoroughly cleaning the glass substrate with an ultrasonic bath of isopropyl alcohol, acetone, and clean air. In the second step, the CAuS were fabricated by using 20 μl of $HAuCl_4$ dissolved in 20 ml of ethylene glycol. This solution was heated to 70 °C for 24 h and cooled down for 24 h at room temperature. The solution was then centrifuged to sediment the CAuS and replace the ethylene glycol with acetone. This process was repeated four times to ensure the CAuS were dispersed primarily in acetone. In the third step we spin coated the glass substrate with the CAuS solution at 2000 rpm for 1 min. Finally, the glass substrate was baked at 100 °C for 1 h to evaporate any remaining acetone.

2.2. Near-field imaging

To image the iPRP, we used a near-field scanning optical microscope (Nanonics Multiview 1500) in collection mode with a ∼300 nm apertured probe. The instrument was capable of simultaneously mapping the sample topography and the light intensity in the near-field. We used a scan resolution of 512 points per line. In our setup, the near-field probe and the excitation spot were at fixed positions while the sample was scanned across the x- and y-directions. A linearly polarized laser source with a wavelength of $\lambda_0 = 660$ nm was used to excite and measure the iPRP. The illumination of the sample was set to the back of the substrate, normal to its surface. The incident beam was focused with a 5× objective lens to a spot size of ∼100 μm diameter, centered at the position of the near-field probe. We selected this spot size to generate a uniform field over the measured areas. This way, the iPRP would be visible as an interference pattern in the near-field intensity. It is important to mention that we selected near-field microscopy since this technique has proven to detect mostly in-plane interactions [10]. Figure 1(a) shows a schematic representation of our experimental setup.

2.3. Numerical model

In order to further support our experimental results, we developed numerical models based on the finite element method. Our models emulated our experimental conditions, i.e. the shapes and sizes of the CAuS, the illumination conditions, and the materials. We limited the study region to a cylinder surrounded by perfect matching layers that absorbed the scattered fields. The CAuS were located at the center of the region. We simulated three structures, that coincide with our experimental findings, as described in the Results section.

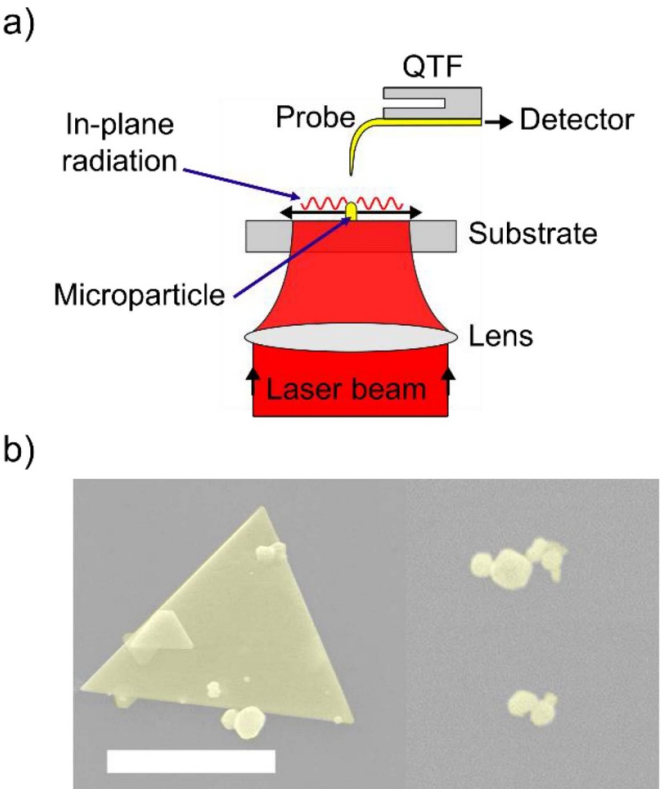

Figure 1. (a) Schematic representation of the experimental setup. (b) Composed false-color electron microscopy image of a set of CAuS. The scale bar represents 5 μm.

These structures were a symmetric particle, an asymmetric particle, and a triangular flake. In the case of a single particle, the simulation domain had 11 μm of diameter, while for the triangular flake, the diameter was 17 μm. We used a wavelength of 660 nm and linear polarization to follow the experimental conditions.

3. Results

3.1. CAuS

Due to the nature of the fabrication process, we found that the CAuS are mostly particles and flakes with triangular and hexagonal symmetries. Figure 1(b) shows a representative set of CAuS. As it is clear, the size of the structures ranges from hundreds of nanometers to tens of microns. For this particular work, we selected structures with dimensions ranging from ∼2 λ_0 to ∼10 λ_0, i.e. from ∼1 μm to ∼7 μm. This selection was chosen to demonstrate that particles with dimensions larger than the wavelength can efficiently radiate in the plane of the sample surface.

3.2. In-plane radiation pattern

We selected two kinds of structures to measure the iPRP: particles and triangular flakes. In all cases reported, the polarization of the excitation field was set in the horizontal

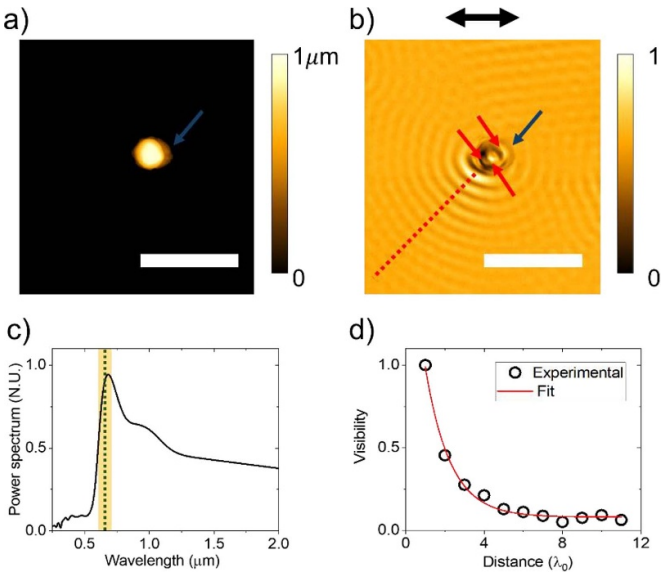

Figure 2. (a) Topography of an individual Au particle with 1.8 μm diameter. (b) Normalized intensity of the iPRP. In both cases, the scale bar represents 5 μm. The black arrow in (b) represents the polarization of the excitation field. (c) The fourier transform of the intensity profile taken along the dashed line in (b). The dashed line on graph (c) represents the excitation wavelength, and the yellow shade represents the uncertainty of the experimental wavelength. (d) Experimental visibility (open circles) and theoretical fit (red line) measured at the red dashed line in (b).

direction. We describe the iPRPs generated by particles and flakes in separate subsections for clearer analysis and interpretation.

3.2.1. Particles. Figure 2(a) shows the topography of an isolated Au particle with a diameter of 1.44 μm ($\sim$2.2 λ_0) and a height of 0.80 μm. Figure 2(b) shows the normalized intensity of the iPRP the Au particle in figure 2(a) generated. Due to the particle topography, it is clear that the iPRP generated was asymmetric. We found that the bump in the particle, see blue arrow in figure 2(a), suppressed the iPRP in the direction of the bump. We believe this was due to the disruption on the surface of the particle, which launched the radiation in a direction that the near-field probe could not detect. It was also interesting to find that there were some modes on the surface of the particle. We believe that these modes are surface plasmons due to the Au properties [18]. In particular, it is clear in figure 2(b) that there is a peak surrounded by two lobes on the intensity at the top of the Au particle, see the red arrows. We believe these features displayed a plasmonic resonance, due to the size of the top region, the direction of the polarization, and the nature of the particle. Furthermore, these features could represent the first plasmonic resonant mode in a quasi-circular cavity [19].

As seen in figure 2(b), the iPRP was visualized as an interference pattern generated by the superposition of the incoming excitation light and the iPRP itself. We determined the wavelength of the iPRP by calculating the Fourier transform of the intensity profile along the red dashed line in figure 2(b). The result is shown in figure 2(c). As expected, the peak wavelength matched the excitation wavelength, which was within the uncertainty of our experimental wavelength ($\sim$30 nm), as seen with the yellow shade in figure 2(c). This was an expected result since we measured the light scattered by the particle, i.e. this was a linear process.

In order to determine the propagation properties of the iPRP, we measured the intensity decay as a function of the propagation distance. We calculated the visibility per wavelength of the iPRP as visibility $= (I_{\max} - I_{\min}) / (I_{\max} + I_{\min})$ with the result shown in figure 2(d). We found that the best fitting function was a decaying exponential, with decay constant 1.75 $\lambda_0 \pm 0.11$ λ_0, instead of a hyperbolic function of the form $1/r^2$, as one would expect from a radiating source [12]. This finding suggested that the dissipation channel was mainly due to the refractive index contrast between the substrate (glass) and the superstrate (air), confirming the in-plane nature of the detected intensity. In order to allow the iPRP to propagate longer, the refractive index contrast must be reduced to the point in which the substrate and superstrate are made of the same material; unfortunately, this was not possible under our current experimental conditions.

It is worth mentioning that the particle in figure 2(a) had a similar structure to those observed in figure 1(b). However, due to the geometry of the near-field probe, the shape of the mapped topography looked more like a truncated cone with a hemispherical region at the top. This had consequences for the mapping of the intensity on the surface of the particle, as already discussed.

Once we characterized the iPRP generated by a single Au particle, we explored the interaction between the iPRP generated by several particles whose distance is close enough to register interaction among them and longer than the exponential decay constant. This was another way to confirm the in-plane nature of the interactions studied in this work, meaning, if we observe interference among the iPRP generated by independent particles, the radiation is proven to be in plane. Figure 3(a) shows the topography of a set of Au particles separated by $\sim$7 λ_0, violet arrow, and $\sim$6 λ_0, green arrow. Figure 3(b) shows the normalized intensity of the interactions between the iPRPs generated by each particle. As expected, the in-plane interactions created interference patterns that resulted in a focal point, as one would expect from an in-plane interaction, see the blue arrow in figure 3(b).

3.2.2. Triangular flake. The nature of the iPRP from a flake is different from the particle, since its surface was flat, and its lateral dimensions were large compared to the excitation wavelength, $>$4 λ_0. Because of these differences, the near-field probe could map its surface more reliably. Figure 4(a) shows the topography of a triangular Au crystal and two particles, and figure 4(b) shows their iPRP. As expected, the particles generated in-plane patterns similar to those shown in figures 2 and 3 while the flake generated flat wavefronts instead of circular ones as in the case of the particles. This

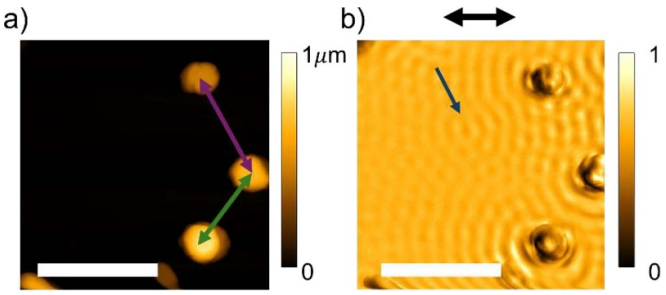

Figure 3. (a) Topography of a set of particles in a semicircle arrangement. (b) Normalized intensity of the interaction of the in-plane radiation generated by the particles in (a). In both cases, the scale bar represents 5 μm. The black arrow in (b) represents the polarization of the excitation field.

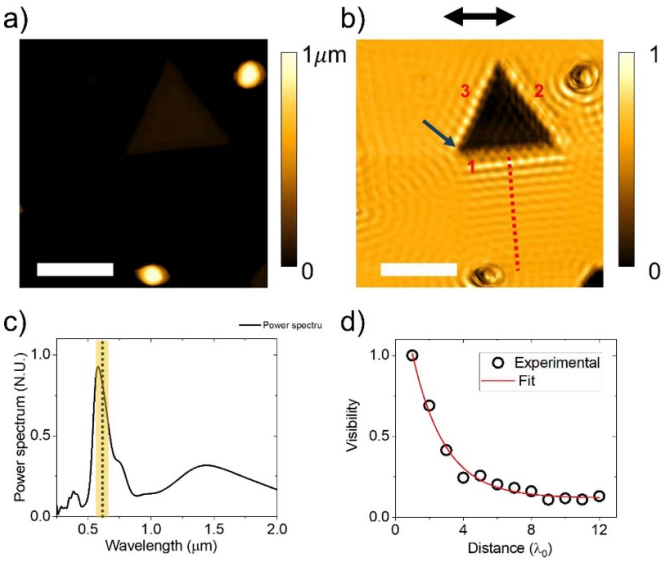

Figure 4. (a) Topography of one Au triangular crystal and two particles. (b) Normalized intensity of the interaction of the iPRP generated by the particles in (a). In both cases, the scale bar represents 5 μm. The black arrow in (b) represents the polarization of the excitation field. (c) Fourier transform of the intensity profile taken along the dashed line in (b). The dashed line represents the excitation wavelength, and the yellow shade represents the uncertainty of the experimental wavelength. (d) Experimental visibility (open circles) and theoretical fit (red line) measured at the red dashed line in (b).

was an expected result due to the shape and dimensions of the edges of the flake.

The triangular crystal we studied had sides of length $\sim$10 λ_0. We have labeled the edges of the crystal for an easier understanding of our analysis. As seen in figure 4(b), edge 1 radiated efficiently into the in-plane direction, while edges 2 and 3 were primarily responsible for the generation of surface plasmons on the surface of the flake. This was an expected result, as the Au flake is thick enough ($\sim$70 nm) to support surface plasmons [18]. Edge 1 was parallel to the polarization, meaning it could not excite surface plasmons, so there were no interference lines parallel to this edge on the surface of the flake, see figure 4(b). We also calculated the wavelength of the iPRP generated by the flake and found that it was similar to the excitation wavelength, as seen in figure 4(c). Finally, we confirmed that the intensity decay in this case was also exponential, as discussed before for the particles, with a decay constant of 1.57 $\lambda_0 \pm 0.11$ λ_0, see figure 4(d), further confirming our previous findings.

An additional interesting finding was the iPRP generated by the corner located between edge 1 and 2, see blue arrow in figure 4(b). Such an iPRP was characterized by a decay constant of 2.5 $\lambda_0 \pm 0.11$ λ_0. We believe that this was due to the shape of such a corner, that as shown in previous studies [20], could be very sharp, resulting in a highly directional in-plane radiation, i.e. an antenna-like structure.

3.3. Numerically calculated results

Figure 5 shows the normalized numerically calculated intensity generated by a symmetric particle, figures 5(a) and (b), a particle with a defect, figures 5(c) and (d), and a triangular flake, figures 5(e) and (f). In figures 5(a), (c), and (e), the normalized intensity is displayed at the surface of the air-glass/gold interfaces, while figures 5(b), (d), and (f) display isometric views. In all cases, the scale bar represents 5 μm, the double arrow is the polarization direction, and the red dashed lines are the edges of the Au structures. We also separated the discussion of particles and the flake into two sections for an easier understanding of the results.

3.3.1. Particles. Although in our experiments we did not report a non-deformed particle, we performed the calculation of a symmetric particle to determine the origin of the iPRP. As one would expect, the iPRP was symmetric around the particle with no deformation, see figure 5(a). More importantly, in the isometric view (figure 5(b)) we found that the in-plane radiation pattern was generated by the scattering at the bottom edges of the particle. Interestingly, the strongest radiation happens in the direction perpendicular to the polarization. We believe this happened because the energy in the direction parallel to the polarization was primarily coupled into surface plasmons on the surface of the particle, see blue arrow in figure 5(b). In addition, we found that the calculated iPRP presented an exponential decay with decay constant $\sim$2.25 λ_0 for this non-deformed particle.

In the case of the deformed particle, the presence of the perturbation on the surface of the particle generated an asymmetric pattern, see figure 5(c). It can be seen that the iPRP was quite similar to that reported in figure 2(b), see blue arrow in figure 5(c). It was also interesting that the particle displayed resonant modes on its surface, see blue arrow in figure 5(d); however, the intensity of these resonant modes was not as strong as in the case of the symmetric particle. In this case, the iPRP was also generated by the scattering at the bottom edges of the particle and its decay constant was $\sim$2 λ_0.

In both cases, the decay constant was certainly larger than that measured experimentally. We believe that this was due to

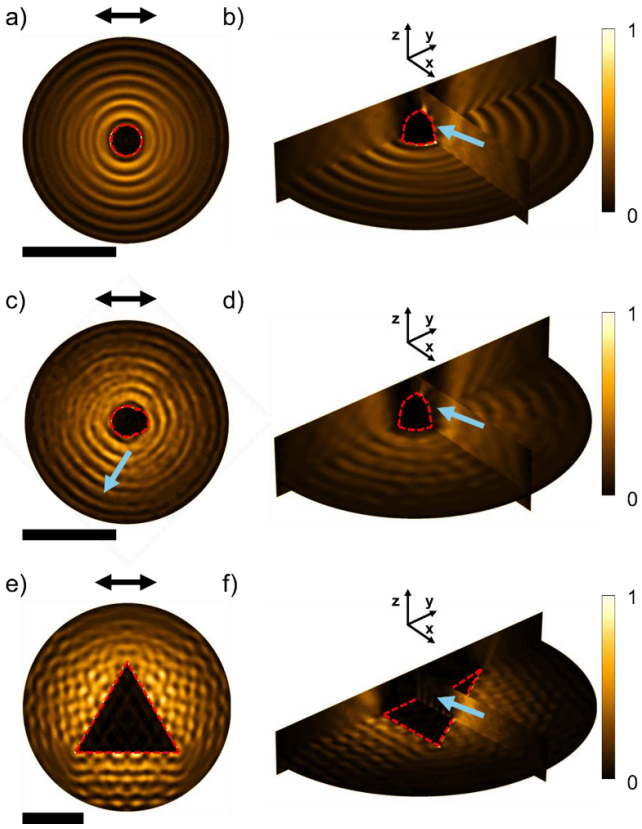

Figure 5. Numerically calculated normalized intensity of a Au particle without defect, a Au particle with defect, and a Au triangular flake. (a), (c), and (e) Show the top view and (b), (d), and (f) show the isometric view. In all cases, the scale bar represents 5 μm.

several factors not considered in the numerical simulations, among them, the finite roughness of the glass substrate, the uncertainty in the angle of incidence of the excitation field, and the effect of the near-field probe.

3.3.2. Triangular flake. The numerically calculated iPRP generated by a triangular flake, figure 5(e), is quite similar to our experimental results reported in figure 4(b); the plasmonic modes that are visible in the surface of the crystal in figures 5(e) and (f), were only generated by the edges which were not parallel to the polarization, as expected. It is clear from figure 5(e) that the calculated iPRP generated by the triangular flake was symmetric with respect to the edges 1, 2, and 3, in correspondence with figure 4(b). This means that each edge radiated the same amount of energy. However, it is important to mention that our model did not take into account the anisotropic nature of the edges of the Au flakes [14], i.e. all the edges were simulated as vertical walls. We believe that it could be possible for the radiation efficiency to be dependent on the geometry of the Au flake edges and the uncertainty in our reported direction of the excitation field. In this case, we also found that the origin of the iPRP was the scattering at the bottom edges of the flake, as aforementioned.

4. Conclusions

In summary, we have shown that large Au particles and flakes with dimensions larger than the excitation wavelength are able to generate in-plane radiation. According to our findings, the iPRPs had exponential behavior due to the refractive index contrast between the substrate and the superstrate. The origin of the iPRP was found to be the scattering of the excitation field at the bottom edges of the CAuS, confirmed by the existence of surface plasmons on the surface of the Au structures. In addition, we found that the iPRPs can interact under adequate conditions. The good agreement between our experimental results and the reported numerical simulations gives us confidence that our findings are correctly addressed. Our results open a new venue for the control of in-plane interactions even without using the well-known surface plasmon polaritons or the tight constraints of subwavelength PAs.

Data availability statement

All data that support the findings of this study are included within the article (and any supplementary files).

Acknowledgment

J M Merlo acknowledges Vassar College for the startup funding with Number ST00027.

Conflict of interest

The authors declare no conflicts of interest

ORCID iD

Juan M Merlo https://orcid.org/0000-0002-3956-0940

References

[1] Alù A and Engheta N 2010 Wireless at the nanoscale: optical interconnects using matched nanoantennas *Phys. Rev. Lett.* **104** 213902
[2] Giannini V, Fernández-Domínguez A I, Heck S C and Maier S A 2011 Plasmonic nanoantennas: fundamentals and their use in controlling the radiative properties of nanoemitters *Chem. Rev.* **111** 3888–912
[3] Habib A, Zhu X, Fong S and Yanik A A 2020 Active plasmonic nanoantenna: an emerging toolbox from photonics to neuroscience *Nanophotonics* **9** 3805–29
[4] Hongwei J and Haitao L 2015 Role of surface plasmon polaritons and other waves in the radiation of resonant optical dipole antennas *Sci. Rep.* **4** 8456
[5] Takafumi S, Yanazawa K, Maeda S, Hofmann H F and Kadoya Y 2014 Radiation pattern of plasmonic nano-antennas in a homogeneous medium *Opt. Express* **11** 13263–8
[6] Markus P and Lukas N 2019 Optical antennas driven by quantum tunneling: a key issues review *Rep. Prog. Phys.* **82** 112401

[7] Hassan M M, Sium F S, Islam F and Choudhury S M 2021 A review on plasmonic and metamaterial based biosensing platforms for virus detection *Sens. Bio-Sens. Res.* **33** 100429
[8] Dos Santos P S S, De Almeida J M M M, Pastoriza-Santos I and Coelho L C C 2021 Advances in plasmonic sensing at the NIR—a review *Sensors* **21** 2111
[9] Shang X, Niu J, Wang C, Li L, Lu C, Zhang Y and Shi L 2022 Mie resonances enabled subtractive structural colors with low-index-contrast silicon metasurfaces *ACS Appl. Mater. Interfaces* **14** 55933–43
[10] Merlo J M, Nesbitt N T, Calm Y M, Rose A H, D'Imperio L, Yang C, Naughton J R, Burns M J, Kempa K and Naughton M J 2016 Wireless communication system via nanoscale plasmonic antennas *Sci. Rep.* **6** 31710
[11] Bellanca G, Calò G, Kaplan A E, Bassi P and Petruzzelli V 2017 Integrated vivaldi plasmonic antenna for wireless on-chip optical communications *Opt. Express* **25** 16214
[12] Dregely D, Lindfors K, Lippitz M, Engheta N, Totzeck M and Giessen H 2014 Imaging and steering an optical wireless nanoantenna link *Nat. Commun.* **5** 4354
[13] Yang Y, Li Q and Qiu M 2024 Broadband nanophotonic wireless links and networks using on-chip integrated plasmonic antennas *Sci. Rep.* **6** 19490
[14] Curto A G, Volpe G, Taminiau T H, Kreuzer M P, Quidant R and van Hulst N F 2010 Unidirectional emission of a quantum dot coupled to a nanoantenna *Science* **329** 930–3
[15] Ho J, Fu Y H, Dong Z, Paniagua-Dominguez R, Koay E H H, Yu Y F, Valuckas V, Kuznetsov A I and Yang J K W 2018 Highly directive hybrid metal−dielectric Yagi-Uda nanoantennas *ACS Nano* **12** 8616–24
[16] Han D, Deng S, Ye T and Wei Y 2023 Enhancement of pattern quality in maskless plasmonic lithography via spatial loss modulation *Microsyst. Nanoeng.* **9** 40
[17] Horák M, Bukvišová K, Švarc V, Jaskowiec J, Křápek V and Šikola T 2018 Comparative study of plasmonic antennas fabricated by electron beam and focused ion beam lithography *Sci. Rep.* **8** 9640
[18] Merlo J M, Rhoads C and Carhart M H 2023 Anisotropic generation and detection of surface plasmon polaritons using near-field apertured probes *IEEE Photon. J.* **15** 4800405
[19] Ye F, Burns M J and Naughton M J 2013 Plasmonic halos—optical surface plasmon drumhead modes *Nano Lett.* **13** 519–23
[20] Boroviks S, Wolff C, Linnet J, Yang Y, Todisco F, Roberts A S, Bozhevolnyi S I, Hecht B and Mortensen N A 2018 Interference in edge-scattering from monocrystalline gold flakes *Opt. Mater. Express* **8** 3688